

Photoelectrochemical hydrogen production from water splitting using heterostructured nanowire arrays of Bi₂O₃/BiAl oxides as a photocathode

Pedro E.A. Salomão^a, Danielle S. Gomes^a, Everson J.C. Ferreira^b, Francisco Moura^b,
Lucas L. Nascimento^c, Antônio O.T. Patrocínio^c, Márcio C. Pereira^{a,*}

^a Institute of Science, Engineering, and Technology (ICET), Federal University of the Jequitinhonha and Mucuri Valleys (UFVJM), Campus Mucuri, Teófilo Otoni 39803-371, Minas Gerais, Brazil

^b Federal University of Itajubá (UNIFED), Campus Itabira, Itabira 35903-087, Minas Gerais, Brazil

^c Institute of Chemistry, Federal University of Uberlândia (UFU), Uberlândia 38400-902, Minas Gerais, Brazil



ARTICLE INFO

Keywords:

Solar energy
Water reduction
PEC cells
Spray pyrolysis
Heterojunction
Oxides

ABSTRACT

To date, most metal oxide-based photocathodes used in photoelectrochemical cells for water splitting contain copper cations in its composition, which can be reduced to metal Cu under cathodic bias leading to deactivation of the photoelectrode. Here, a Cu-free photocathode composed by a ternary heterostructure of Bi₂O₃/Al₂Bi₂₄O₃₉/Al₂Bi₄₈O₇₅ nanowires is reported with a narrow band gap energy (1.83 eV) and suitable conduction band edge potential (−0.98 V_{RHE}) for water reduction to hydrogen. Photoelectrochemical measurements display that the highest photocurrent density of −4.85 mA cm^{−2} at 0 V_{RHE} under simulated sunlight is achieved by tuning the Bi:Al molar ratio of photocathode to 21:1. The photocurrent onset potential of the Bi₂O₃/BiAl oxides photoelectrode was estimated to be 0.57 V_{RHE} at pH 7, which is comparable to that of silicon. Controlled potential photoelectrolysis at 0 V_{RHE} showed a stable photocurrent of about −2 mA cm^{−2} for 2 h of continuous operation. The H₂ measured at this time was 696 μmol cm^{−2}, which corresponds to a Faradaic efficiency of 93%. Finally, this work gives a new generation of Cu-free photocathodes and demonstrates a promising future of BiAl oxides in constructing photoelectrochemical devices for water splitting.

1. Introduction

Hydrogen fuel production from sunlight and water in photoelectrochemical (PEC) devices is a promising approach to supply renewable and carbon-free energy [1–3]. In PEC devices, the photoanode (n-type semiconductor) and/or photocathode (p-type semiconductor) use light to produce oxygen and hydrogen from water splitting, respectively [4–9]. A techno-economic analysis shows that the cost of hydrogen produced by silicon solar cells with a solar-to-hydrogen (STH) efficiency of 9.8% still is expensive compared to the hydrogen produced by steam reforming of natural gas [10]. Therefore, new earth-abundant semiconductors need to be synthesized with less cost than crystalline silicon, while sustaining high STH efficiency and stability.

Earth-abundant n-type metal oxides such as BiVO₄ (E_g = 2.4 eV) [11–17], Fe₂O₃ (2.2 eV) [18–22], ZnO [23,24], and WO₃ (2.6 eV) [25–27] have been widely studied as photoanodes, while p-type Cu₂O (2.0 eV) [28–31], CuBi₂O₄ (1.5 eV) [32–35], and CuFeO₂ (1.5 eV) [36–38] have been used as photocathodes in PEC cells. Metal oxide photoelectrodes have the advantage of simpler synthesis methods than

its non-oxide counterparts, but they have commonly smaller optical absorption coefficients, poor charge-carrier mobility, and short charge-carrier-lifetime, which results in lower photocurrents and energy conversion [29]. Notably, most p-type metal oxides utilized in PEC cells contain copper, which is known to cause the deactivation of Cu-based photocathodes due to copper reduction under cathodic bias [28]. Thus, the development of new p-type photoelectrodes that do not contain copper in its composition is of interest.

Bismuth-based oxides are good alternatives to make visible-light photocathodes [39] due to their electronic structures are formed by hybridized Bi 6s and O 2p orbitals in the valence band, which favors the good dispersion of charge carriers and decreases the band gap energy [39]. However, to date, a limited number of Bi-based oxide photocathodes can perform photoelectrochemical hydrogen evolution, including α-Bi₂O₃ [40], CuBi₂O₄ [41–45], BaBiO₃ [46], BiFeO₃ [47], and Bi₂FeCrO₆ [48]. Among these Bi-based photocathodes, CuBi₂O₄ exhibits the better photoelectrochemical performance for H₂ evolution from water splitting due to its small bandgap energy in the range of 1.5–1.8 eV, conduction band with a more negative potential than the

* Corresponding author.

E-mail address: marcio.pereira@ufvjm.edu.br (M.C. Pereira).

<https://doi.org/10.1016/j.solmat.2018.12.037>

Received 30 September 2018; Received in revised form 7 December 2018; Accepted 28 December 2018

Available online 02 January 2019

0927-0248/© 2018 Elsevier B.V. All rights reserved.

reduction potential of H^+/H_2 , and photocurrent onset potential near $+1 V_{RHE}$. Although, $CuBi_2O_4$ undergoes photocorrosion in aqueous electrolyte due to Cu reduction, which limits its practical use as a photocathode [35,41].

Here we demonstrate a p-type Cu-free photoelectrode composed by a ternary heterostructure of $Bi_2O_3/Al_2Bi_{24}O_{39}/Al_2Bi_{48}O_{75}$ nanowires fabricated by spray pyrolysis, exhibiting a small band gap energy ($E_g = 1.83 eV$), a proper conduction band edge potential ($-0.98 V_{RHE}$) for proton reduction at neutral pH, and a high cathodic photocurrent for photoelectrochemical water splitting. The role of Bi/Al ratio on the photoabsorption and PEC performance is also assessed.

2. Materials and methods

2.1. Fabrication of photocathodes

Five photoelectrodes composed of Al_2O_3 , Bi_2O_3 , and composites of BiAl oxides with Bi:Al molar ratios of 14:1, 21:1, and 23:1 were prepared. The photoelectrodes were fabricated on conductive fluorine-doped tin oxide (FTO)-coated glass substrates ($10 mm \times 20 mm \times 2 mm$, $16 \Omega cm^{-2}$), previously cleaned in an ultrasonic bath using acetone and ethanol. Before deposition, two different solutions of Al and Bi were made by dissolving 20 mmol Al ($(NO_3)_3 \cdot 9H_2O$ (solution 1) and 20 mmol $Bi(NO_3)_3 \cdot 5H_2O$ (solution 2) each in 100 mL glacial acetic acid (99.7%) under stirring at $60^\circ C$ for 40 min. The solutions were directly sprayed down onto the FTO glass substrates at $130^\circ C$ using a commercial airbrush (0.3 mm nozzle) at 14 cm distance of FTO, with 20 cycles of spray deposition for 5 s. Then, the substrates were annealed in a muffle furnace at $500^\circ C$ for 2 h in an air atmosphere to produce crystalline films of Al_2O_3 and Bi_2O_3 . The precursor solutions 1 and 2 were mixed to achieve Bi:Al molar ratios of 1:1, 2:1, and 3:1, respectively in order to obtain films of BiAl oxides. Subsequently, the resulting solutions were stirred at $60^\circ C$ for 40 min to form stable and homogeneous solutions. These solutions were used for the film deposition onto FTO as described above. After spray deposition, the films were annealed in air at $500^\circ C$ for 2 h to produce the composite photoelectrodes.

2.2. Characterization of the photocathodes

The structural analysis of the photoelectrodes was carried out by X-ray diffraction (XRD) measurements using an X-ray diffractometer (Rigaku Smartlab, Japan) with a scanning speed of $0.03^\circ min^{-1}$ and $CuK\alpha$ radiation ($\lambda = 1.54056 \text{ \AA}$). The morphology of the films was evaluated by field emission scanning electron microscopy (FE-SEM) using a Supra 35-VP (Carl Zeiss, Germany) microscope. High-resolution transmission electron microscopy (HRTEM) images were collected with an FEI TECNAI G20 F20 microscope operating at 200 kV. The electronic structure of the films was assessed by diffuse reflectance measurements using a UV/Vis spectrophotometer (Cary 5G). MgO was used as reference material (100% transmission). The Bi and Al contents in the films were analyzed by X-ray fluorescence (XRF) spectrometer (Phillips PW 1480).

2.3. Photoelectrochemical measurements

The performance of the photocathodes for water reduction was monitored with a potentiostat (AUTOLAB Potentiostat-Galvanostat PGSTAT 128 N) using a standard three-electrode configuration, with Ag/AgCl (3.0 M KCl) as reference electrode, platinum plate as counter electrode, and Al, Bi, and BiAl oxides as working electrodes with irradiation areas of $0.5 cm^2$, and scan rate of $20 mV s^{-1}$. A 0.5 M Na_2SO_4 aqueous solution (pH 7.2) was used as the electrolyte. The current-potential (J-V) curves were obtained in the dark and under simulated solar spectrum generated by a Xe source (Xenolux 300). The light intensity of the xenon lamp was calibrated to 1 sun ($100 mW cm^{-2}$) using

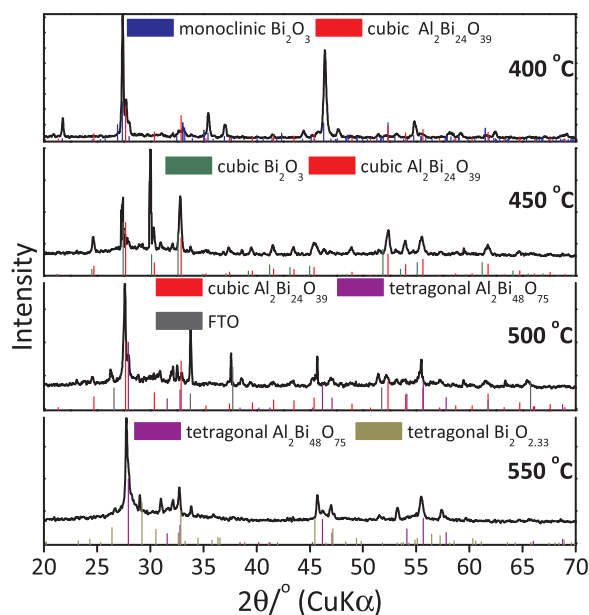


Fig. 1. XRD patterns of the photocathodes produced by spray pyrolysis of the precursor of Bi:Al solutions with a molar ratio of 1:1 at $130^\circ C$ and annealing at different temperatures.

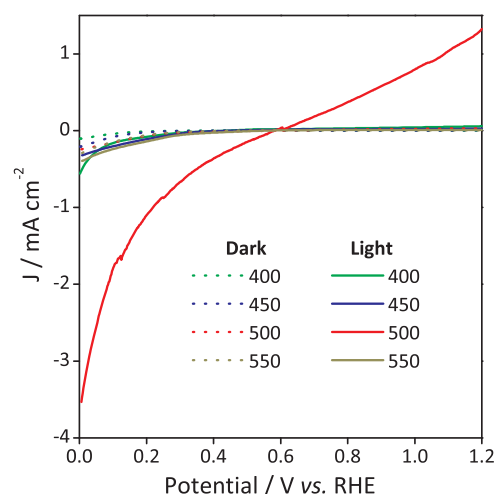


Fig. 2. Current density-potential curves collected from low to high potentials for the photocathodes produced by spray pyrolysis of Bi:Al solutions with molar ratio of 1:1 at $130^\circ C$ and annealing at different temperatures. Measurement conditions: illuminated area = $0.5 cm^2$, 0.5 M Na_2SO_4 electrolyte (pH = 7.2), light source = 300 W Xe lamp ($100 mW cm^{-2}$), scan rate = $20 mV s^{-1}$, back illumination for all photocathodes.

a pyranometer (APG-MP-200). For converting the obtained potential versus Ag/AgCl to RHE, Eq. (1) was used:

$$E_{RHE} = E_{Ag/AgCl} + 0.059pH + 0.197 \quad (1)$$

The electrochemical impedance spectra (EIS) were obtained using a potentiostat-galvanostat (AUTOLAB PGSTAT 128 N) equipped with the FRA32M module. The Nyquist plots were measured at 0 V vs. RHE with an AC amplitude of 20 mV, frequency of 100 kHz – 100 mHz in the dark and under a $100 mW cm^{-2}$ Xe light. The 0.5 M Na_2SO_4 solution was used as the electrolyte. The EIS data were fitted with NOVA 1.11 software.

The incident photon-to-current efficiency (IPCE) spectra of Bi:Al films were calculated from photocurrent measurements in a two-electrode configuration using the Eq. (2).

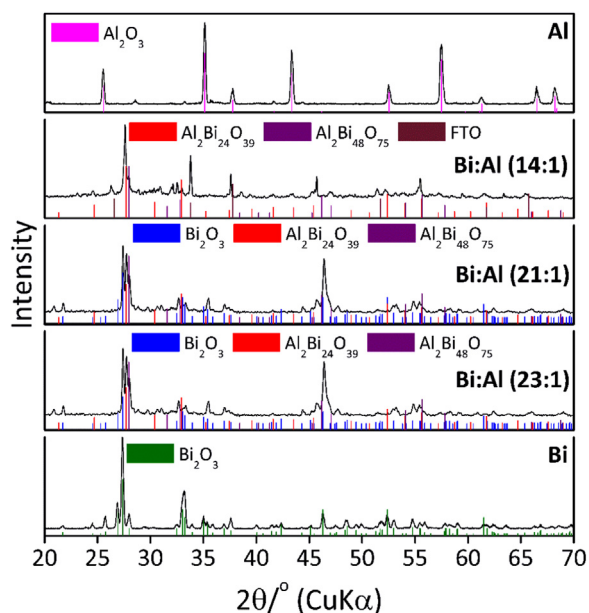


Fig. 3. XRD patterns of the photocathodes produced by spray pyrolysis of different Bi:Al molar ratio at 130 °C and subsequent annealing at 500 °C.

$$\text{IPCE} = \frac{(1240 \text{ eV nm}) I_{\text{ph}}}{\lambda P_{\text{irr}}} \quad (2)$$

The I_{ph} is the photocurrent density in mA cm^{-2} , λ is the wavelength of the incident radiation in nm, and the P_{irr} is the incident photon flux in mW cm^{-2} . The light excitation was performed using a 300 W Xe lamp in a Newport/Oriel housing. The photon flux was determined by a Newport 1919-R power meter equipped with an 818-UV/DB sensor before and after photocurrent measurements. The Bi:Al films were used as photocathodes and a platinumized FTO as the counter electrode. 0.5 M Na_2SO_4 was used as the electrolyte.

2.4. Faradaic efficiency for H_2 and O_2 evolution

The faradaic efficiency measurements were performed by using Unisense hydrogen (H2-500), and oxygen (OX-500) probes controlled by a Microsensor Multimeter (4-CH) with sensor trace Logger software. The amperometric H_2 measurements were carried out by using an H_2 microsensor connected to a multimeter polarized at +1 V for 1 h. After a stable current in the pA range was achieved, the microsensor was ready for use. For calibration, high-purity H_2 gas was bubbled through the 0.5 M Na_2SO_4 solution until H_2 saturation was reached. Then, the H_2 -saturated Na_2SO_4 solution was diluted to various concentrations in a calibration chamber. The current was estimated from the average of the data points taken during each measurement. The detection limit for H_2 using the microsensors is 0.3 μM . The O_2 microsensor was pre-polarized at -0.8 V for 2 h and calibrated with a CAL300 (Unisense) microprobe calibration chamber. Finally, the H_2 and O_2 produced in the photocathode and counter-electrode was divided by the theoretical amount of hydrogen and oxygen gas respectively to obtain the faradaic efficiency.

3. Results and discussion

The photoelectrodes used in this study were fabricated by spray pyrolysis of Bi:Al solutions. First, precursor solutions with Bi:Al molar ratio of 1:1 were deposited at 130 °C directly on FTO-coated glass substrates and then annealed at different temperatures to evaluate the effect of phase formation on the photoelectrochemical performance of the photocathodes. The X-ray diffraction (XRD) pattern of the as-grown Bi:Al particles at 400 °C (Fig. 1) indicate the formation of monoclinic $\alpha\text{-Bi}_2\text{O}_3$ (JCPDS File No. 41-1449) and cubic $\text{Al}_2\text{Bi}_{24}\text{O}_{39}$ (JCPDS File No.

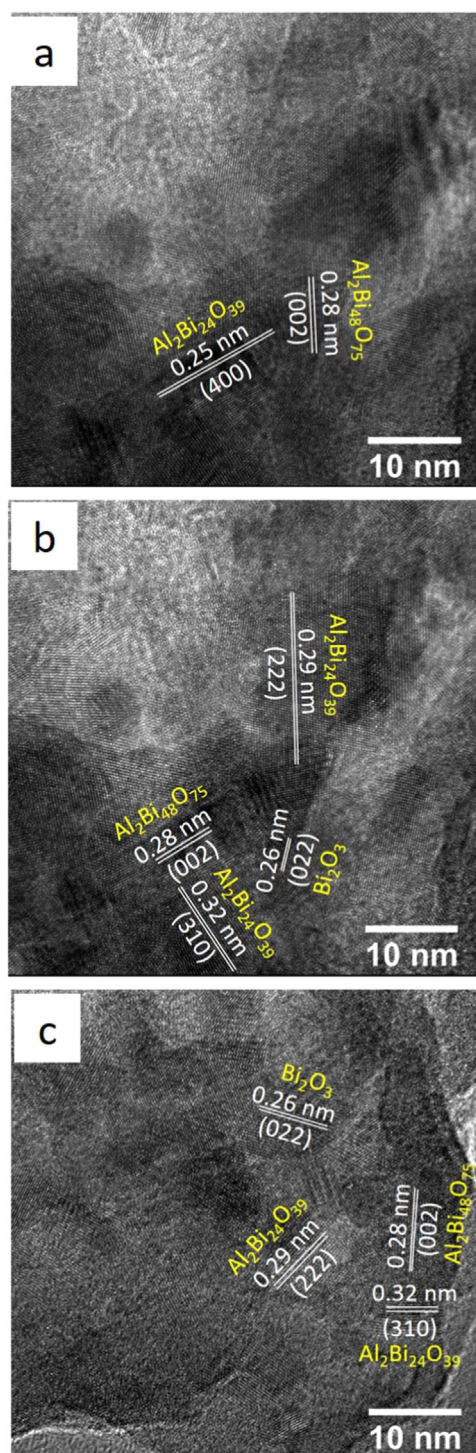


Fig. 4. High-resolution transmission electron microscopy (HRTEM) image of a. Bi:Al (14:1), b. Bi:Al (21:1), and c. Bi:Al (23:1) photocathodes.

42-184) as a minority phase. At 450 °C, cubic $\gamma\text{-Bi}_2\text{O}_3$ (JCPDS File No. 45-1344) and cubic $\text{Al}_2\text{Bi}_{24}\text{O}_{39}$ (JCPDS File No. 42-184) were the phases formed. The photocathodes produced at 500 °C are constituted by cubic $\text{Al}_2\text{Bi}_{24}\text{O}_{39}$ (JCPDS File No. 42-184) and tetragonal $\text{Al}_2\text{Bi}_{48}\text{O}_{75}$ (JCPDS File No. 42-199), while tetragonal $\beta\text{-Bi}_2\text{O}_3$ (JCPDS File No. 42-199) and tetragonal $\text{Al}_2\text{Bi}_{48}\text{O}_{75}$ are produced at 550 °C.

To evaluate the photoelectrochemical activity of the heterostructures above for water reduction, we employ the as-grown Bi:Al films as the photocathodes. The photocurrent density versus potential ($J \times V$) curves (Fig. 2) were obtained under simulated sunlight

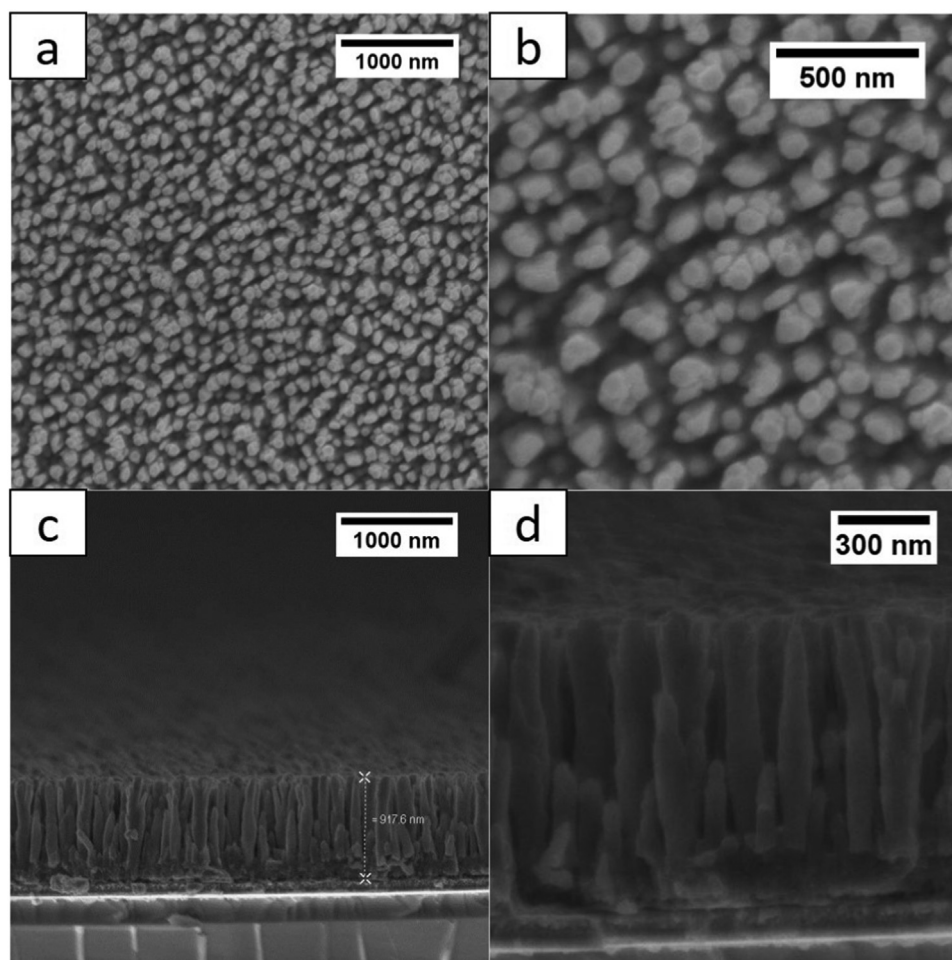


Fig. 5. (a, b) Top-view and (c, d) cross-section SEM images of Bi:Al (21:1) photocathode.

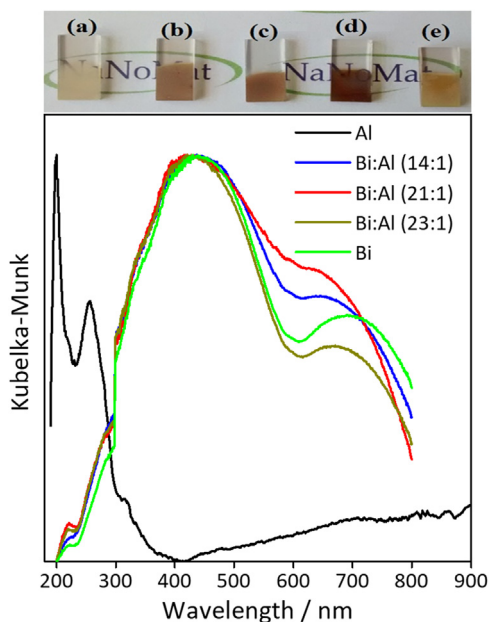


Fig. 6. UV-Vis diffuse reflectance spectra of Bi:Al photocathodes. (a) Al_2O_3 , (b) Bi:Al (41:1), (c) Bi:Al (21:1), (d) Bi:Al (23:1), (e) Bi_2O_3 .

illumination at 100 mW cm^{-2} from a 300 W Xe lamp using a conventional three-electrode configuration. The photocurrent density

measured at 0 V_{RHE} for the photocathode annealed at 500°C (-3.29 mA cm^{-2}) was significantly higher than the photocurrents produced by other heterojunctions annealed at 400°C (-0.45 mA cm^{-2}), 450°C (-0.12 mA cm^{-2}), and 550°C (-0.11 mA cm^{-2}), respectively, suggesting the coupling between $\text{Al}_2\text{Bi}_{24}\text{O}_{39}$ and $\text{Al}_2\text{Bi}_{48}\text{O}_{75}$ favors the photoelectrochemical water reduction. It should be observed that the photocurrent density described in this work corresponds to the difference between the current densities obtained under illumination and in the dark at 0 V_{RHE} .

Subsequently, the photocathode annealed at 500°C was optimized by varying the Bi:Al molar ratios of the precursor solutions used for the film deposition. Hence, three photoelectrodes were fabricated by spray pyrolysis of solutions with initial Bi:Al molar ratios of 1:1, 2:1, and 3:1 at 130°C followed by annealing in air at 500°C for 2 h. The Bi and Al contents determined by XRF was found to be 88.3 wt% Bi and 0.8 wt% Al for the Bi:Al (1:1), 88.8 wt% Bi and 0.6 wt% Al for the Bi:Al (2:1), and 88.9 wt% Bi and 0.5 wt% Al for the Bi:Al (3:1), which correspond to Bi:Al molar ratios of 14:1, 21:1, and 23:1, respectively. It suggests the Bi is preferentially spray deposited on the FTO-coated glass substrates because it is much heavier than Al. Thus, the films were labeled Bi:Al (14:1), Bi:Al (21:1), and Bi:Al (23:1). The XRD patterns of the photoelectrodes (Fig. 3) revealed the photocathode Bi:Al (14:1) is formed by cubic $\text{Al}_2\text{Bi}_{24}\text{O}_{39}$ (JCPDS File No. 42-184) and tetragonal $\text{Al}_2\text{Bi}_{48}\text{O}_{75}$ (JCPDS File No. 42-199). Increasing the Bi content in the Bi:Al (21:1) and Bi:Al (23:1) photoelectrodes results in the formation of monoclinic $\alpha\text{-Bi}_2\text{O}_3$ (JCPDS File No. 41-1449) in addition to $\text{Al}_2\text{Bi}_{24}\text{O}_{39}$ and $\text{Al}_2\text{Bi}_{48}\text{O}_{75}$ phases. The formation of $\text{Bi}_2\text{O}_3/\text{AlBi}$ heterojunctions was evidenced by HRTEM (Fig. 4). The lattice fringes of $d = 0.26 \text{ nm}$ and d

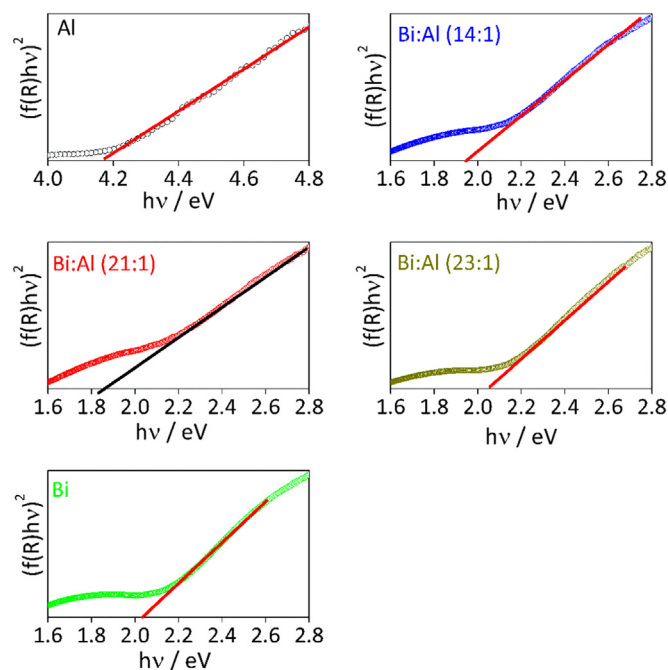


Fig. 7. Tauc's plots for the Al, Bi:Al (14:1), Bi:Al(21:1), Bi:Al (23:1), and Bi photocathodes. For the band gap determination, the diffuse reflectance data were used. The fraction of light transmitted was measured as reflectance, and the Kubelka-Munk radiative transfer model was employed to extract α . In this model, $f(R) = \frac{(1-R)^2}{2R} = \frac{\alpha}{s}$, where $f(R)$ is the Kubelka-Munk function and s is the scattering coefficient. If the scattering coefficient is wavelength independent, then $f(R)$ is proportional to α , and the Tauc plots can be made using $f(R)$ in the place of α .

= 0.29 nm agree well with the crystallographic planes of α - Bi_2O_3 (022) and $\text{Al}_2\text{Bi}_{48}\text{O}_{75}$ (002), respectively. The d values of 0.25, 0.29, and 0.32 nm correspond to the (400), (222), and (310) planes of $\text{Al}_2\text{Bi}_{24}\text{O}_{39}$, respectively. Fig. 5 shows the SEM images of the top- and cross-sectional views of Bi:Al (21:1) film. The heterostructured photocathode presents self-organized nanowire arrays with a mean diameter of 100 nm and length of about 920 nm.

For comparison, photoelectrodes composed of bare Al_2O_3 and Bi_2O_3 were also prepared by spray pyrolysis of solutions of Al and Bi at 130 °C followed by annealing in air at 500 °C for 2 h. The XRD patterns (Fig. 3) confirmed the rhombohedral and monoclinic structures of Al_2O_3 and

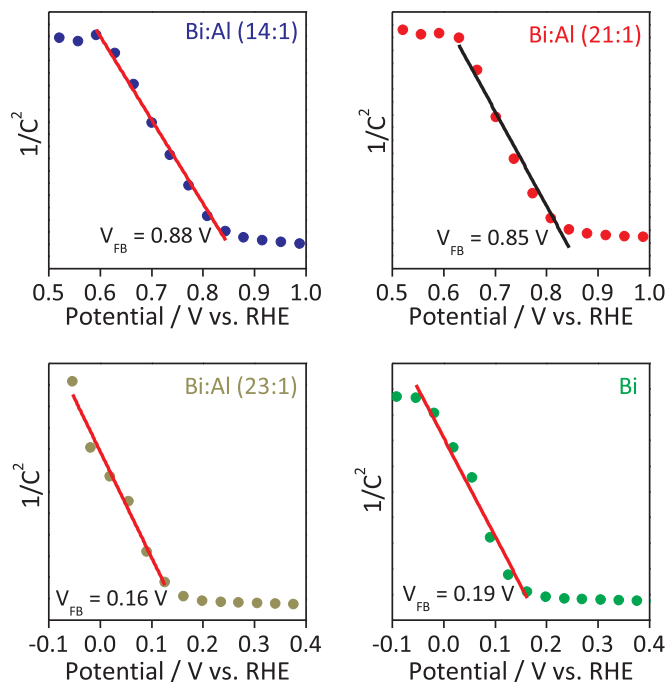


Fig. 9. Mott-Schottky plots for the bare Bi_2O_3 and Bi:Al heterostructures obtained at 1 kHz. The measurement was done in 0.5 M Na_2SO_4 (pH = 7.2) in the dark.

Bi_2O_3 according to the JCPDS Files No. 46–1212 and 41–1449, respectively.

UV–vis diffuse reflectance spectra of Al_2O_3 , Bi_2O_3 , and the different Bi:Al heterostructures (Fig. 6) were collected to assess the optical absorption features of the films. The Al_2O_3 film absorbs light in the ultraviolet region as evidenced by the two intense absorption bands centered at 199 and 256 nm. On the other hand, the Bi and Bi:Al films absorb light over a wide range of wavelengths, from 800 to 200 nm. The optical band gap energies of Al_2O_3 , Bi:Al (14:1), Bi:Al (21:1), Bi:Al (23:1), and Bi_2O_3 films estimated from the Tauc plots (Fig. 7) were 4.17, 1.92, 1.83, 2.03, and 2.02 eV, respectively. Thus, the theoretical maximum photocurrent densities from the AM 1.5 G spectrum expected for the Bi:Al (14:1), Bi:Al (21:1), Bi:Al (23:1), and Bi_2O_3 films are approximately 16.5, 18.8, 13.9, and 14.1 mA cm^{-2} , respectively.

The $J \times V$ plots of Al_2O_3 , Bi_2O_3 , and Bi:Al heterojunctions are shown in Fig. 8a. The Al_2O_3 photoelectrode shows no photoactivity

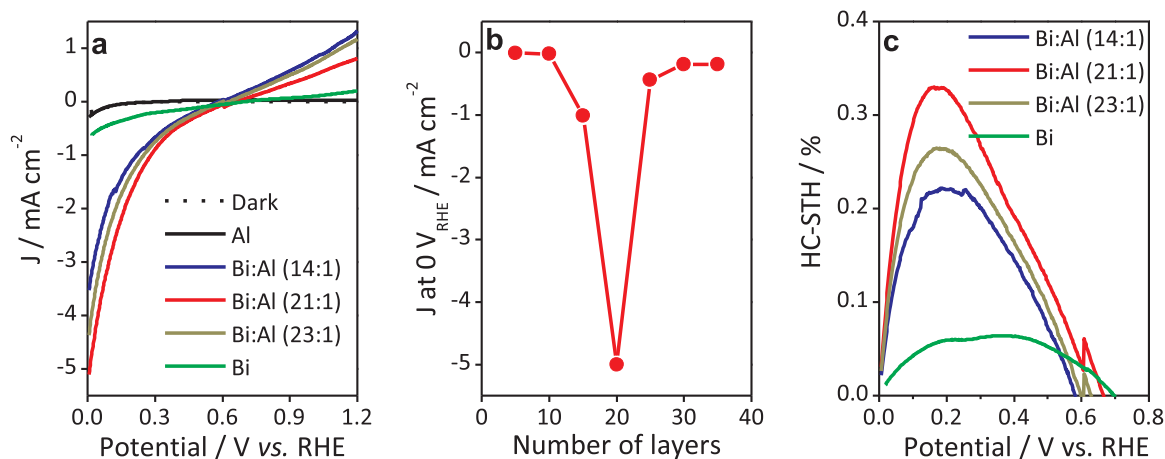


Fig. 8. (a) J - V plots obtained using three-electrode cells for the Bi:Al photocathode. (b) Photocurrent density as a function of the number of layers of Bi:Al (21:1) films. (c) HC-STH efficiency for the Bi:Al photocathodes. Measurement conditions: active area = 0.25 cm^2 , 0.5 M Na_2SO_4 electrolyte (pH 7.2), Xe light (100 mW cm^{-2}), scan rate = 20 mW s^{-1} , back illumination for all photocathodes.

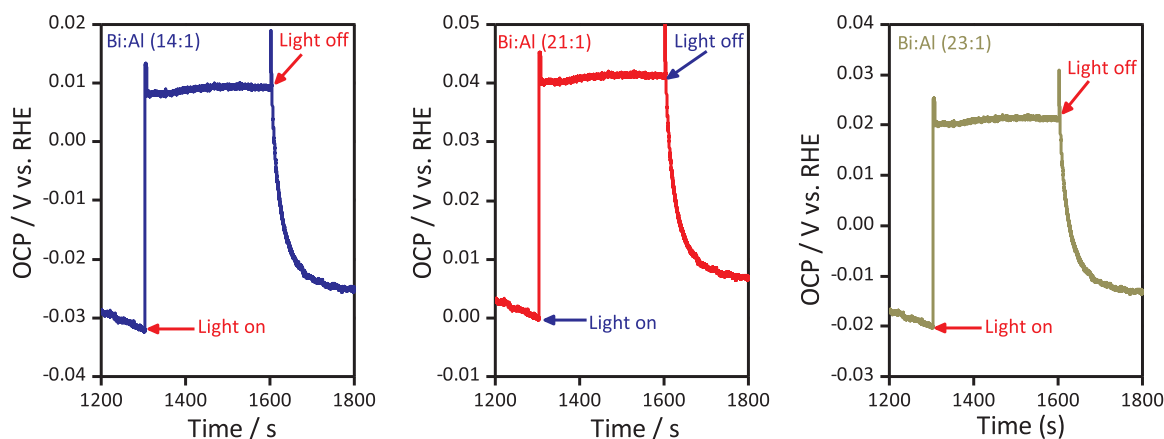


Fig. 10. Open circuit potential measurements of Bi:Al photocathodes. Measurement conditions: active area of 1 cm², 0.5 M Na₂SO₄/0.1 M K₃Fe(CN)₆/0.1 M K₄Fe(CN)₆ electrolyte, light source: Xe (100 mW cm⁻²).

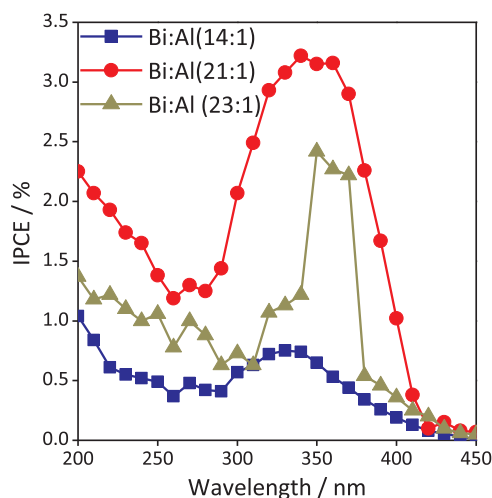


Fig. 11. IPCE spectra of Bi:Al films collected at -0.6 V vs. Pt in 0.5 M Na₂SO₄ under front-side illumination.

under the studied conditions. On the other hand, the cathodic photocurrents of Bi₂O₃ and Bi:Al heterojunctions increased as the potential was swept into the negative direction, which suggests the p-type nature

of the photoelectrodes. The Mott-Schottky plots for the Bi₂O₃ and Bi:Al photoelectrodes (Fig. 9), in which 1/C² (C = capacitance of the space charge layer) is plotted against the potential, gave straight lines with negative slopes corresponding to accumulation regions typical of p-type semiconductors. The conductivity type of films can also be determined by OCP measurements. If OCP shifts towards more anodic potentials (positive) under illumination, the film is p-type. If OCP moves towards more cathodic potentials (negative) under illumination, the film is n-type [49]. Thus, the positive shift in OCP of Bi:Al photoelectrodes (Fig. 10) upon illumination confirms the films have p-type conductivity. The photocurrent onset potentials (E_{onset}) of Bi:Al (14:1) (0.53 V_{RHE}), Bi:Al(21:1) (0.57 V_{RHE}), and Bi:Al (23:1) (0.54 V_{RHE}) heterojunctions estimated at current density of -0.1 mA cm⁻² (Fig. 8a) for the water reduction were higher than that determined for Bi₂O₃ (E_{onset} = 0.51 V_{RHE}). Therefore, the Bi₂O₃ film produced the lowest photocurrent density of -0.54 mA cm⁻² at 0 V_{RHE}, while the highest photocurrent of -4.85 mA cm⁻² was obtained with the Bi:Al (21:1) photoelectrode followed by Bi:Al (23:1) (-4.13 mA cm⁻²) and Bi:Al (14:1) (-3.29 mA cm⁻²).

Fig. 8b displays the photocurrent of Bi:Al (21:1) photocathode at 0 V_{RHE} as a function of film thickness under illumination. Films of 920 nm (20 layers) provided the highest photocurrent under 100 mW cm⁻² light irradiation. It is due to the strong correlation between light absorption and charges transport with the film thickness. Increasing the

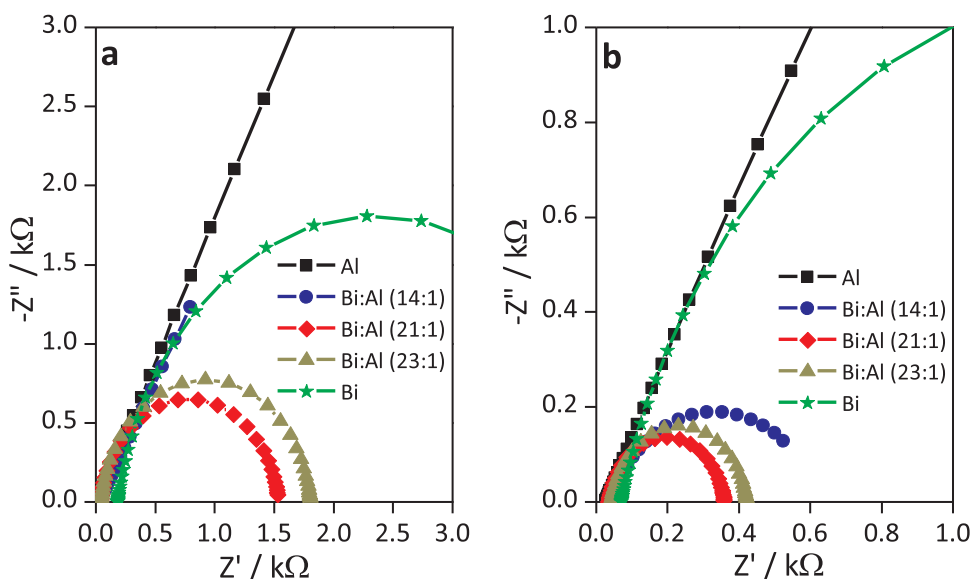


Fig. 12. Electrochemical impedance spectra of Bi:Al photocathodes at 0 V_{RHE} (a) in the dark and (b) under illumination at a frequency range of 100 mHz–10 kHz. Measurement conditions: active area = 0.25 cm², 0.5 M Na₂SO₄ electrolyte (pH 7.2), Xe light (100 mW cm⁻²), scan rate = 20 mW s⁻¹, back illumination for all photocathodes.

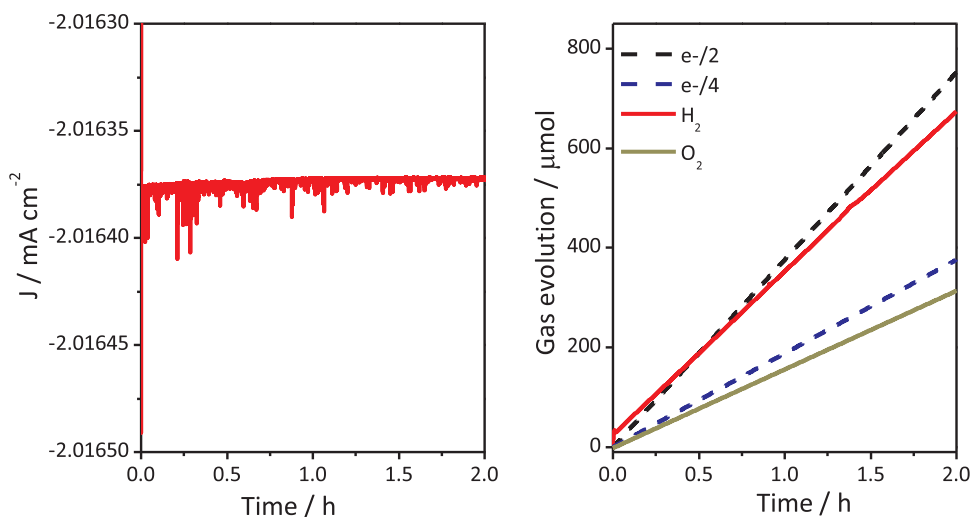


Fig. 13. (a) Stability test for the Bi:Al (21:1) photocathode polarized at 0 V_{RHE} using a three-electrode cell setup. (b) H_2 evolved in the Bi:Al (21:1) photocathode. The black and blue dotted lines represent the amount of H_2 and O_2 expected for a faradaic efficiency of 100% (For interpretation of the references to color in this figure legend, the reader is referred to the web version of this article).

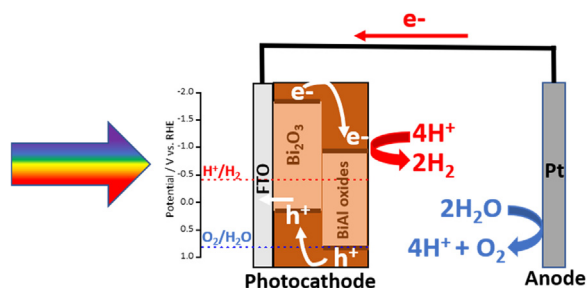


Fig. 14. Schematic representation of the water-splitting PEC cell and working principle of the BiAl oxides photocathode under illumination.

film thickness increases the light absorption but simultaneously decreases the charge separation. On the other hand, decreasing the film thickness increases the charge separation but decreases the light absorption. Thus, 920 nm is the optimal thickness that balances both light absorption and charges separation.

Energy conversion of the bare Bi_2O_3 and Bi:Al photocathodes were estimated by calculating their half-cell solar-to-hydrogen (HC-STH) efficiencies using Eq. (2) [50].

$$HC-STH = |J|(E - E_{H^+/H_2}) \times 100 / P_{sun} \quad (2)$$

where J is the photocurrent density, E is the applied potential, E_{H^+/H_2} is the equilibrium redox potential of hydrogen (0 V_{RHE}), and P_{sun} is the power density of the incident light (100 mW cm^{-2}). As shown in Fig. 8c, the Bi:Al (21:1) photocathode had the highest HC-STH of 0.33% at 0.16 V_{RHE} . At the same potential, the Bi:Al (23:1), Bi:Al (14:1), and Bi_2O_3 photocathodes achieved HC-STH efficiencies of 0.27%, 0.22%, and 0.05%, respectively.

The IPCE spectra of Bi:Al films collected at -0.6 V vs. Pt in a two-electrode setup are shown in Fig. 11. The Bi:Al (21:1) film exhibited the highest IPCE value of 3.2% at 340 nm against 2.39% at 350 nm of Bi:Al (23:1) and 0.73% at 330 nm of Bi:Al (14:1) films.

The kinetics of charge transfer in the photocathodes was evaluated by electrochemical impedance spectroscopy (EIS) measurements. The charge transfer resistance (R_{ct}) of films under illumination (Fig. 12b) was significantly smaller than those obtained in the dark (Fig. 12a) due to higher electron conductivity of photocathodes under light irradiation. Among the photoelectrodes, Al_2O_3 exhibited the higher R_{ct} of 110 and 67 $k\Omega$ in the dark and under illumination, respectively, followed by the Bi_2O_3 film that presented R_{ct} values of 25 $k\Omega$ in the dark and 2.5 $k\Omega$ under light irradiation. Notoriously, the Bi:Al heterojunctions showed the lowest R_{ct} values, following the order: Bi:Al (21:1) (1.5 $k\Omega$ in the

dark; 0.3 $k\Omega$ under illumination) < Bi:Al (23:1) (1.7 $k\Omega$ in the dark; 0.4 $k\Omega$ under illumination) < Bi:Al (14:1) (1.8 $k\Omega$ in the dark and 0.93 $k\Omega$ under light illumination).

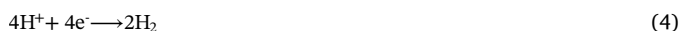
To further investigate the stability of Bi:Al (21:1) film, the short-term stability was investigated by a standardized protocol in which the controlled-current water splitting is monitored by chronoamperometry measurements for 2 h of continuous operation [51]. The Bi:Al (21:1) photocathode showed a stable photocurrent of approximately -2 mA cm^{-2} at 0 V_{RHE} for 2 h of continuous operation under light irradiation (Fig. 13a), which corresponds to an H_2 production of $752 \mu\text{mol cm}^{-2}$ according to Faraday's law (Fig. 13b). To evaluate whether the obtained cathodic photocurrent comes from the hydrogen generation rather than any other undesirable side reactions, in situ determination of the hydrogen evolved was carried out by using Unisense hydrogen (H_2-500) probes controlled by a Microsensor Multi-meter (4-CH) with sensor trace Logger software. The amount of H_2 measured in situ was equal to $696 \mu\text{mol cm}^{-2}$ in 2 h (Fig. 13b). Thus, the Faradaic efficiency is estimated to be 93%, which confirms that the photocurrent indeed comes from the water reduction reaction. The O_2 production in the counter-electrode was also monitored by oxygen (OX-500) probe. The amount of O_2 generated in the counter-electrode was $322 \mu\text{mol cm}^{-2}$, which corresponds to a Faradaic efficiency of about 87%. Thus, the overall water splitting is the primary reaction that takes place in the photoelectrochemical cell. The Bi and Al contents determined by ICP-MS in the electrolyte after the photoelectrochemical tests were smaller than $0.05 \mu\text{g L}^{-1}$, suggesting the photocathode is stable against photocorrosion under the studied conditions. To the best of our knowledge, Bi_2O_3 /BiAl ternary oxide photocathode exhibited a stable photocurrent density at 0 V_{RHE} and pH 7 superior to those reported to date for Bi-based photocathodes such as α - Bi_2O_3 [40], $CuBi_2O_4$ [41–45], $BaBiO_3$ [46], $BiFeO_3$ [47], and Bi_2FeCrO_6 [48], which makes the BiAl photocathodes promising for constructing PEC devices for water splitting.

The proposed mechanism for the water-splitting PEC cell operation at pH 7 under back-side illumination is shown in Fig. 14. Under simulated sunlight, electrons and holes are generated in the BiAl photocathode. From the Mott-Schottky measurements and DRS data, it was seen that the conduction band (CB) level and valence band (VB) of Bi_2O_3 are more negative than the corresponding bands of BiAl oxides, which favors the band-to-band charge transfer. Thus, electrons from the CB of Bi_2O_3 are injected into CB of BiAl oxides while holes in the VB of BiAl oxides are transferred to the VB of Bi_2O_3 , improving the charge separation in the photocathode. Indeed, the $J \times V$ curves (Fig. 8a) showed that the ternary heterostructure of BiAl oxides is photoelectrochemically more efficient than the bare Bi_2O_3 or binary heterostructure of BiAl oxides for water splitting. After photogeneration and

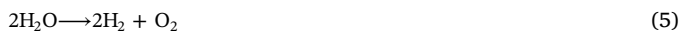
separation of charges, the photoexcited holes in photocathode are transferred to the Pt anode and oxidize water to form O_2 and H^+ ions (Eq. (3)):



Then, the H^+ ions formed in the half-reaction of water oxidation migrate to the photocathode and are reduced to form H_2 (Eq. (4)). It should be noted that the pH of the electrolyte was unchanged during the photoelectrochemical tests.



Thus, the overall water splitting (Eq. (5)) is the primary reaction in the PEC cell. H_2 and O_2 are produced with 93% and 87% Faradaic efficiency.



4. Conclusions

A Cu-free photocathode composed by a ternary heterostructure of $Bi_2O_3/Al_2Bi_{24}O_{39}/Al_2Bi_{48}O_{75}$ nanowires with a small band gap energy ($E_g = 1.83$ eV) and suitable conduction band edge potential ($-0.98 V_{RHE}$) for the proton reduction to hydrogen under simulated sunlight was synthesized for the first time by spray pyrolysis. We found that the photoelectrochemical performance of the photocathode can be tuned by changing the Bi:Al molar ratio in the precursor solution. PEC measurements revealed that the highest photocurrent of -4.85 mA cm^{-2} at $0 V_{RHE}$ and pH ≈ 7 was achieved for the Bi:Al (21:1) photocathode, which exhibited the highest photocurrent onset of $0.57 V_{RHE}$ and lowest charge transfer resistance of 0.3 k Ω under illumination. The HC-STH efficiency of Bi:Al (21:1) photocathode was estimated to be 0.33% at $0.16 V_{RHE}$. Controlled photoelectrolysis experiments at $0 V_{RHE}$ show a stable photocurrent of -2 mA cm^{-2} for 2 h of continuous operation. The measured hydrogen production was estimated to be $696 \mu mol cm^{-2}$, which corresponds to a Faradaic efficiency of 93% . Finally, this approach provides insights into a new generation of Cu-free photocathodes for photoelectrochemical water splitting.

Acknowledgements

This work was supported by CNPq (grant numbers 442820/2014-3; 304598/2014-3; 301839/2017-4; INCT MIDAS), FAPEMIG (grant numbers REDE-113/10; CEX-RED-00010-14; APQ-00369-14; RED00520-16; CEX-112-10; PPM-00104-17), FINEP, and CAPES, Brazil.

References

- [1] S.K. Saraswat, D.D. Rodene, R.B. Gupta, Recent advancements in semiconductor materials for photoelectrochemical water splitting for hydrogen production using visible light, *Renew. Sust. Energy Rev.* 89 (2018) 228–248.
- [2] J. Qi, W. Zhang, R. Cao, Solar-to-hydrogen energy conversion based on water splitting, *Adv. Energy Mater.* 8 (2018) 1701620.
- [3] C. Jiang, S.J. Moniz, A. Wang, T. Zhang, J. Tang, Photoelectrochemical devices for solar water splitting—materials and challenges, *Chem. Soc. Rev.* 46 (2017) 4645–4660.
- [4] K. Sivula, Metal oxide photoelectrodes for solar fuel production, surface traps, and catalysis, *J. Phys. Chem. Lett.* 4 (2013) 1624–1633.
- [5] L.J. Mingguo, W.R.W. Daud, M.B. Kassim, An overview of photocells and photo-reactors for photoelectrochemical water splitting, *Int. J. Hydrog. Energy* 35 (2010) 5233–5244.
- [6] K. Zhang, M. Ma, P. Li, D.H. Wang, J.H. Park, Water splitting progress in tandem devices: moving photolysis beyond electrolysis, *Adv. Energy Mater.* 6 (2016) 1600602.
- [7] M.G. Walter, E.L. Warren, J.R. McKone, S.W. Boettcher, Q. Mi, E.A. Santori, N.S. Lewis, Solar water splitting cells, *Chem. Rev.* 110 (2010) 6446–6473.
- [8] S.Y. Reece, J.A. Hamel, K. Sung, T.D. Jarvi, A.J. Esswein, J.J. Pijpers, D.G. Nocera, Wireless solar water splitting using silicon-based semiconductors and earth-abundant catalysts, *Science* 334 (2011) 645–648.
- [9] J. Li, N. Wu, Semiconductor-based photocatalysts and photoelectrochemical cells for solar fuel generation: a review, *Catal. Sci. Technol.* 5 (2015) 1360–1384.
- [10] M.R. Shaner, H.A. Atwater, N.S. Lewis, E.W. McFarland, A comparative technoeconomic analysis of renewable hydrogen production using solar energy, *Energy Environ. Sci.* 9 (2016) 2354–2371.
- [11] W.S. dos Santos, M. Rodriguez, J.M. Khoury, L.A. Nascimento, R.J. Ribeiro, J.P. Mesquita, A.C. Silva, F.G. Nogueira, M.C. Pereira, Bismuth vanadate photoelectrodes with high photovoltage as photoanode and photocathode in photoelectrochemical cells for water splitting, *ChemSusChem* 11 (2018) 589–597.
- [12] A.T. Oliveira, M. Rodriguez, T.S. Andrade, H.E. de Souza, J.D. Ardisson, H.S. Oliveira, L.C. Oliveira, E. Lorençon, A.C. Silva, L.L. Nascimento, High water oxidation performance of W-doped $BiVO_4$ photoanodes coupled to V_2O_5 rods as a photoabsorber and hole carrier, *Sol. RRL* 8 (2018) 1800089.
- [13] W.S. dos Santos, L.D. Almeida, A.S. Afonso, M. Rodriguez, J.P. Mesquita, D.S. Monteiro, L.C. Oliveira, J.D. Fabris, M.C. Pereira, Photoelectrochemical water oxidation over fibrous and sponge-like $BiVO_4/\beta-Bi_4V_2O_{11}$ photoanodes fabricated by spray pyrolysis, *Appl. Catal. B-Environ.* 182 (2016) 247–256.
- [14] W.S. Dos Santos, M. Rodriguez, A.S. Afonso, J.P. Mesquita, L.L. Nascimento, A.O. Patrocínio, A.C. Silva, L.C. Oliveira, J.D. Fabris, M.C. Pereira, A hole inversion layer at the $BiVO_4/Bi_4V_2O_{11}$ interface produces a high tunable photovoltage for water splitting, *Sci. Rep.* 6 (2016) 31406.
- [15] I.D. Sharp, J.K. Cooper, F.M. Toma, R. Buonsanti, Bismuth vanadate as a platform for accelerating discovery and development of complex transition-metal oxide photoanodes, *ACS Energy Lett.* 2 (2016) 139–150.
- [16] H.L. Tan, R. Amal, Y.H. Ng, Alternative strategies in improving the photocatalytic and photoelectrochemical activities of visible light-driven $BiVO_4$: a review, *J. Mater. Chem. A* 5 (2017) 16498–16521.
- [17] Y. Park, K.J. McDonald, K.-S. Choi, Progress in bismuth vanadate photoanodes for use in solar water oxidation, *Chem. Soc. Rev.* 42 (2013) 2321–2337.
- [18] Y.W. Phuan, W.-J. Ong, M.N. Chong, J.D. Ocon, Prospects of electrochemically synthesized hematite photoanodes for photoelectrochemical water splitting: a review, *J. Photoch. Photobiol. C* 33 (2017) 54–82.
- [19] S. Shen, S.A. Lindley, X. Chen, J.Z. Zhang, Hematite heterostructures for photoelectrochemical water splitting: rational materials design and charge carrier dynamics, *Energy Environ. Sci.* 9 (2016) 2744–2775.
- [20] K. Sivula, F. Le Formal, M. Grätzel, Solar water splitting: progress using hematite ($\alpha-Fe_2O_3$) photoelectrodes, *ChemSusChem* 4 (2011) 432–449.
- [21] D.K. Bora, A. Braun, E.C. Constable, “In rust we trust”. Hematite—the prospective inorganic backbone for artificial photosynthesis, *Energy Environ. Sci.* 6 (2013) 407–425.
- [22] D. Chen, Z. Liu, M. Zhou, P. Wu, J. Wei, Enhanced photoelectrochemical water splitting performance of $\alpha-Fe_2O_3$ nanostructures modified with Sb_2S_3 and cobalt phosphate, *J. Alloy. Compd.* 742 (2018) 918–927.
- [23] Z. Liu, J. Zhang, W. Yan, Enhanced photoelectrochemical water splitting of photoelectrode simultaneous decorated with cocatalysts based on spatial charge separation and transfer, *ACS Sustain. Chem. Eng.* 6 (2018) 3565–3574.
- [24] J. Han, Z. Liu, K. Guo, B. Wang, X. Zhang, T. Hong, High-efficiency photoelectrochemical electrodes based on $ZnIn_2S_4$ sensitized ZnO nanotube arrays, *Appl. Catal. B-Environ.* 163 (2015) 179–188.
- [25] C.A. Bignozzi, S. Caramori, V. Cristino, R. Argazzi, L. Meda, A. Tacca, Nanostructured photoelectrodes based on WO_3 : applications to photooxidation of aqueous electrolytes, *Chem. Soc. Rev.* 42 (2013) 2228–2246.
- [26] T. Zhu, M.N. Chong, E.S. Chan, Nanostructured tungsten trioxide thin films synthesized for photoelectrocatalytic water oxidation: a review, *ChemSusChem* 7 (2014) 2974–2997.
- [27] J. Zhang, Z. Liu, Z. Liu, Novel WO_3/Sb_2S_3 heterojunction photocatalyst based on WO_3 of different morphologies for enhanced efficiency in photoelectrochemical water splitting, *ACS Appl. Mater. Interfaces* 8 (2016) 9684–9691.
- [28] I. Sullivan, B. Zoellner, P.A. Maggard, Copper (I)-based p-type oxides for photoelectrochemical and photovoltaic solar energy conversion, *Chem. Mater.* 28 (2016) 5999–6016.
- [29] Q. Huang, Z. Ye, X. Xiao, Recent progress in photocathodes for hydrogen evolution, *J. Mater. Chem. A* 3 (2015) 15824–15837.
- [30] C.G. Morales-Guio, L. Liardet, M.T. Mayer, S.D. Tilley, M. Grätzel, X. Hu, Photoelectrochemical hydrogen production in alkaline solutions using Cu_2O coated with earth-abundant hydrogen evolution catalysts, *Angew. Chem. Int. Ed.* 54 (2015) 664–667.
- [31] A. Paracchino, V. Laporte, K. Sivula, M. Grätzel, E. Thimsen, Highly active oxide photocathode for photoelectrochemical water reduction, *Nat. Mater.* 10 (2011) 456–461.
- [32] R. Patil, S. Kelkar, R. Naphade, S. Ogale, Low temperature grown $CuBi_2O_4$ with flower morphology and its composite with CuO nanosheets for photoelectrochemical water splitting, *J. Mater. Chem. A* 2 (2014) 3661–3668.
- [33] Y. Nakabayashi, M. Nishikawa, Y. Nosaka, Fabrication of $CuBi_2O_4$ photocathode through novel anodic electrodeposition for solar hydrogen production, *Electrochim. Acta* 125 (2014) 191–198.
- [34] D. Cao, N. Nasori, Z. Wang, Y. Mi, L. Wen, Y. Yang, S. Qu, Z. Wang, Y. Lei, p-Type $CuBi_2O_4$: an easily accessible photocathodic material for high-efficiency water splitting, *J. Mater. Chem. A* 4 (2016) 8995–9001.
- [35] F. Wang, W. Septina, A. Chemseddine, F.F. Abdi, D. Friedrich, P. Bogdanoff, R. van de Krol, S.D. Tilley, S.P. Berglund, Gradient self-doped $CuBi_2O_4$ with highly improved charge separation efficiency, *J. Am. Chem. Soc.* 139 (2017) 15094–15103.
- [36] Y.J. Jang, Y.B. Park, H.E. Kim, Y.H. Choi, S.H. Choi, J.S. Lee, Oxygen-intercalated $CuFeO_2$ photocathode fabricated by hybrid microwave annealing for efficient solar hydrogen production, *Chem. Mater.* 28 (2016) 6054–6061.
- [37] M.S. Prévot, X.A. Jeanbourquin, W.S. Bourée, F. Abdi, D. Friedrich, R. Van De Krol, N. Guijarro, F. Le Formal, K. Sivula, Evaluating charge carrier transport and surface states in $CuFeO_2$ photocathodes, *Chem. Mater.* 29 (2017) 4952–4962.

- [38] Y. Oh, W. Yang, J. Tan, H. Lee, J. Park, J. Moon, Photoelectrodes based on 2D opals assembled from Cu-delfalossite double-shelled microspheres for enhanced photoelectrochemical response, *Nanoscale* 10 (2018) 3720–3729.
- [39] S.S. Bhat, H.W. Jang, Recent advances in bismuth-based nanomaterials for photoelectrochemical water splitting, *ChemSusChem* 10 (2017) 3001–3018.
- [40] R. Sharma, M. Khanuja, S.N. Sharma, O.P. Sinha, Reduced band gap & charge recombination rate in Se doped α - Bi_2O_3 leads to enhanced photoelectrochemical and photocatalytic performance: theoretical & experimental insight, *Int. J. Hydrog. Energy* 42 (2017) 20638–20648.
- [41] S.P. Berglund, F.F. Abdi, P. Bogdanoff, A. Chemseddine, D. Friedrich, R. van de Krol, Comprehensive evaluation of CuBi_2O_4 as a photocathode material for photoelectrochemical water splitting, *Chem. Mater.* 28 (2016) 4231–4242.
- [42] N.T. Hahn, V.C. Holmberg, B.A. Korgel, C.B. Mullins, Electrochemical synthesis and characterization of p- CuBi_2O_4 thin film photocathodes, *J. Phys. Chem. C* 116 (2012) 6459–6466.
- [43] D. Kang, J.C. Hill, Y. Park, K.-S. Choi, Photoelectrochemical properties and photostabilities of high surface area CuBi_2O_4 and Ag-doped CuBi_2O_4 photocathodes, *Chem. Mater.* 28 (2016) 4331–4340.
- [44] G. Sharma, Z. Zhao, P. Sarker, B.A. Nail, J. Wang, M.N. Huda, F.E. Osterloh, Electronic structure, photovoltage, and photocatalytic hydrogen evolution with p- CuBi_2O_4 nanocrystals, *J. Mater. Chem. A* 4 (2016) 2936–2942.
- [45] N. Xu, F. Li, L. Gao, H. Hu, Y. Hu, X. Long, J. Ma, J. Jin, N. Cu-codoped carbon nanosheetnanosheet/Au/ CuBi_2O_4 photocathodes for efficient photoelectrochemical water splitting, *ACS Sustain. Chem. Eng.* 6 (2018) 7257–7264.
- [46] J. Ge, W.-J. Yin, Y. Yan, Solution-processed Nb-substituted BaBiO_3 double perovskite thin films for photoelectrochemical water reduction, *Chem. Mater.* 30 (2018) 1017–1031.
- [47] H. Shen, X. Zhou, W. Dong, X. Su, L. Fang, X. Wu, M. Shen, Dual role of TiO_2 buffer layer in Pt catalyzed BiFeO_3 photocathodes: efficiency enhancement and surface protection, *Appl. Phys. Lett.* 111 (2017) 123901.
- [48] S. Li, B. AlOtaibi, W. Huang, Z. Mi, N. Serpone, R. Nechache, F. Rosei, Epitaxial $\text{Bi}_2\text{FeCrO}_6$ multiferroic thin film as a new visible light absorbing photocathode material, *Small* 11 (2015) 4018–4026.
- [49] Z. Chen, H.N. Dinh, E. Miller, *Photoelectrochemical Water Splitting*, Springer, 2013.
- [50] T. Hisatomi, J. Kubota, K. Domen, Recent advances in semiconductors for photocatalytic and photoelectrochemical water splitting, *Chem. Soc. Rev.* 43 (2014) 7520–7535.
- [51] C.C. McCrory, S. Jung, I.M. Ferrer, S.M. Chatman, J.C. Peters, T.F. Jaramillo, Benchmarking hydrogen evolving reaction and oxygen evolving reaction electrocatalysts for solar water splitting devices, *J. Am. Chem. Soc.* 137 (2015) 4347–4357.